ROYAL SOCIETY OF CHEMISTRY

PAPER

Check for updates

Photocatalytic dissolution of cellulose for hydrogen and nanofiber production: unveiling crucial factors *via* experiments and informatics

Atsushi Kobayashi, [ID] * Atsushi Miura [ID] and Keisuke Takahashi [ID]

The efficient utilization of biomass resources and solar energy is necessary for next-generation sustainable carbon-neutral societies. Although cellulose is the most abundant biomass on Earth, its utilization as a carbon resource is hampered by its strongly stabilized polymer-bundled structure. In this study, a new photoredox cascade catalyst (**PRCC**) conversion system was developed by combining dual-dye-sensitized Pt-cocatalyst-loaded TiO_2 nanoparticle photocatalysts (**DDSP**s) and a 2,2,6,6-tetramethylpiperidine 1-oxyl (TEMPO) oxidation catalyst for the production of cellulose nanofibers and hydrogen from various cellulose substrates (powder, paper, sponge, and wood pellets) under blue light irradiation without the use of strong acids/bases. UV-vis absorption and emission spectroscopy revealed that the loaded amount of the Ru(II) dye on the TiO_2 surface was successfully controlled in the range of 353–667 nmol/1 mg TiO_2, and the immobilization order of two Ru(II) dyes significantly affected the energy- and electron-transfer behaviors between the Ru(II) dyes and TiO_2 nanoparticles. Our systematic evaluation of the photocatalytic activity and machine learning analysis of 12 different **DDSP**s revealed that the immobilization order of the two Ru(II) dyes, full coverage of the TiO_2 nanoparticle surface with suitable Ru(II) dye molecules, and Zr^{4+} cation loading are crucial factors for achieving a high apparent quantum yield for the hydrogen-evolving **PRCC** conversion of cellulose to nanofibers (max. 1.62% at 467 nm excitation for the initial 1 h of reaction in a 0.3 M cellulose aqueous dispersion). The findings contribute to the development of an environmentally benign photocatalytic approach for the conversion of cellulosic biomass as a carbon resource into valuable organic products.

Sustainability spotlight

The efficient utilization of biomass resources as an alternative to fossil fuels is paramount for overcoming global warming and deepening energy crises. Although cellulose is the most abundant biomass resource on earth, its valorisation remains challenging due to the significant economic and environmental costs of overcoming its strongly stabilized polymer-bundled structure. In this work, a photodissolution of cellulose using a photoredox cascade catalyst system comprising a dual-dye-sensitized photocatalyst and a molecular oxidation catalyst is demonstrated to compensate for the energy cost of cellulose depolymerization using sustainable solar energy and to photocatalytically produce both hydrogen and cellulose nanofiber. These correspond to SDGs 7, 9, and 13.

1 Introduction

The efficient utilization of biomass resources as an alternative to fossil fuels is paramount for overcoming global warming and deepening energy crises.[1] Cellulose is the most abundant and sustainable biomass resource on earth and is considered a promising alternative to fossil fuels.[2–7] However, its low solubility in common solvents, originating from its strongly stabilized polymer-bundled structure,[8,9] impedes its widespread utilization. To overcome this drawback, various techniques, including solubilization and hydrolysis using strong bases,[10–12] molten salts,[13] surfactants,[14] and catalytic conversions,[15–19] have

Department of Chemistry, Faculty of Science, Hokkaido University, North-10 West-8, Kita-ku, Sapporo 060-0810, Japan

been established. Among them, the 2,2,6,6-tetramethylpiperidine 1-oxyl (TEMPO)-catalysed oxidation reaction has been extensively studied as an environmentally friendly and powerful technique[17–19] for the production of cellulose nanofiber,[20,21] which has emerged as a promising advanced material in various fields ranging from printable electronics to biomedical applications. However, the valorisation of cellulose remains challenging due to the significant economic and environmental costs of overcoming its strongly stabilized polymer-bundled structure.

Recently, the photocatalytic conversion of cellulose (photoreforming) using solar-light-driven semiconductor photocatalysts has attracted considerable attention[22–29] as it enables the use of renewable sunlight energy to compensate for the energy required for cellulose depolymerization. In their

pioneering work, Kawai and Sakata achieved the photocatalytic decomposition of cellulose using RuO_2- and Pt-co-loaded TiO_2 photocatalysts under 380 nm UV light irradiation to produce H_2 and CO_2 in 0.3% apparent quantum yield (AQY).[30] Since then, numerous TiO_2-based photocatalysts have been developed,[31–35] as well as those based on other semiconductors such as quantum dots[36–38] and carbon nitrides.[39–42] Reisner et. al. recently reported that CdS/CdO_x quantum dots efficiently acted as photocatalysts for H_2 production and cellulose oxidation with a noteworthy AQY of 1.2% under 430 nm visible light irradiation.[36] Nonetheless, to realize the practical application of photocatalytic cellulose conversion, the following drawbacks must be overcome:

(I) Limited utilization of the solar spectrum: Most existing photocatalysts only absorb very limited wavelength regions of sunlight (UV region for TiO_2).

(II) The quantum yields and lifetimes of photoexcited and/or charge-separated states are insufficient to drive the photocatalytic conversion of insoluble cellulose, which is in minimal contact with the photocatalyst surface.

(III) CO_2 emission due to over-oxidation: Semiconductor photocatalysts with a high oxidation potential in the photoexcited state oxidize not only cellulose but also the valuable organic products generated by cellulose oxidation, resulting in CO_2 emission.

(IV) Hazardous reaction conditions, such as the use of strong bases (e.g., NaOH), which are frequently applied to facilitate cellulose depolymerization and to fix the generated CO_2 in aqueous media.

Since the pioneering work by Grätzel et al. on dye-sensitized solar cells,[43–49] the dye sensitization technique has been extensively studied as a promising approach for widening the usable range of the solar spectrum in photovoltaic devices and photocatalysis. The technique allows for both the absorption wavelength and redox potential of the catalyst to be effectively tuned by modifying the molecular structure of the sensitizing dye (photosensitizer = PS). Thus, it offers a promising approach for addressing issues I and III, that is, extending the absorbable wavelength region of solar light and reducing the risk of over-oxidation and reduction. Meanwhile, the recent development of donor-dye-acceptor molecular arrays on semiconductor electrode/catalyst surfaces has enabled significantly improved photoinduced charge separation efficiencies, offering an effective solution to issue II.[50–52] Although the dye-sensitization technique has scarcely been applied to cellulose photoreforming,[31] we recently developed a photo-redox cascade catalyst (PRCC) comprising a dual-dye sensitizing nanoparticulate photocatalyst (DDSP) for hydrogen production and a 2,2,6,6-tetramethylpiperidine 1-oxyl (TEMPO) molecular catalyst for biomass (glycerol and cellulose) reforming.[53] The inclusion of the TEMPO molecular catalyst was found to be effective for enhancing the photocatalyst-cellulose contact, thereby addressing issue II; however, the photocatalytic activity of the developed PRCC system is insufficient (AQY = 0.398% in the initial 1 h of reaction under 460 nm light irradiation).

In this study, we utilized machine learning for the systematic evaluation of a PRCC system wherein the DDSP preparation parameters were extensively varied to identify the DDSP structural parameters that significantly affected the photocatalytic activity. Although machine learning has rarely been applied for analysing dye-sensitized photocatalytic systems,[54,55] we surmised that by significantly streamlining the otherwise arduous and costly structural optimization process, it will enable us to establish an efficient methodology for obtaining highly active PRCCs for solar hydrogen production and cellulose valorisation. Herein, we established that the immobilization order of the two Ru(II) dyes and the Zr^{4+} cation loading on the TiO_2 nanoparticle surface to deliver a stable dual-dye layer structure were crucial for achieving highly efficient photoinduced charge separation in the DDSP and, consequently, the direct photocatalytic conversion of cellulose to nanofiber from the bulk (ranging from wood pellets and paper to fine powder), as well as efficient hydrogen production (AQY = 1.62% at 467 nm excitation during the initial 1 h of the reaction in a 0.3 M cellulose aqueous dispersion). To the best of our knowledge, this is the first photocatalytic system capable of nanofiber production via visible-light-driven photodissolution of cellulose paper under ambient and mild reaction conditions without the use of strong acids or bases.
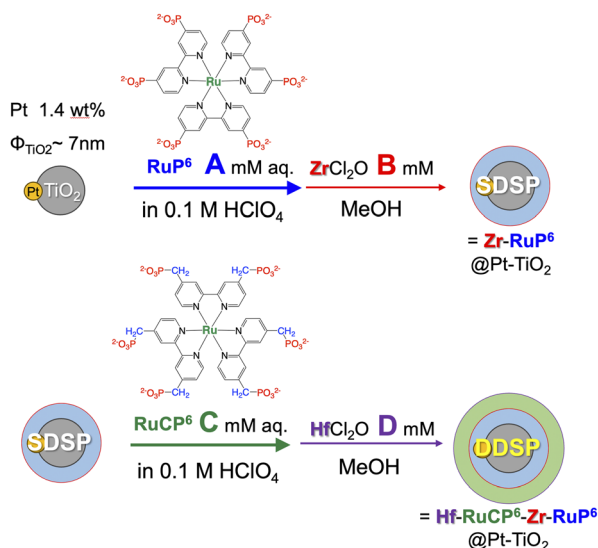
2 Experimental section

2.1 Materials and syntheses

Caution! Although we did not come across any difficulties, most of the chemicals used in this study are potentially harmful and should be used in small quantities and handled with care in a fume hood. All commercially available starting materials were used as received without further purification. The TiO_2 nanoparticles (CSB, ~7 nm in diameter) were purchased from Sakai Chemical Industry Co. Ltd. Pt-TiO_2 (Pt load = 1.34 or 1.38 wt%) was prepared using a previously reported photodeposition method.[56] Ru(II) molecular photosensitizers (RuCP[6] and RuP[6]) were synthesized using previously reported methods and purified on a Sephadex LH-20, eluting with water.[57] A series of dual-dye sensitized Pt-TiO_2 photocatalysts (DDSP-n), Hf^{4+}-RuCP[6]-Zr^{4+}-RuP[6]@Pt-TiO_2, were synthesized by systematical changes in concentrations of RuP[6], RuCP[6], Zr^{4+}, and Hf^{4+} salts in our previous procedure (Scheme 1, and see the SI for details).[58] The immobilized amount of each Ru(II) PS was estimated using the UV-vis absorption spectrum of each supernatant isolated by the ultracentrifugation of the Ru(II) PS immobilization reaction mixture (Fig. S1 and Table S1).

2.2 Measurements

UV-vis absorption spectra were recorded on a JASCO V-750 spectrophotometer. Emission spectra were recorded on a JASCO FP-8550 spectrofluorometer at 298 K and each sample solution was deoxygenated by Ar bubbling for 20 min at 293 K. Energy-dispersive X-ray fluorescence (XRF) spectra were recorded using a Bruker S2 PUMA analyzer. ^{13}C-NMR spectra at room temperature were recorded on an ECZ-400S NMR spectrometer. IR spectra were recorded on a Jasco FT-IR 660 spectrometer equipped with an ATR PRO ONE (with a diamond prism)

Scheme 1 Four-step synthesis of **DDSP-n**.

accessory. The Brownian motion of oxidized cellulose nanoparticles was observed using dark-field microscopy with an inverted microscope (Nikon TE300) equipped with a Plan Fluor 40× objective lens (N.A. 0.6) and a dry dark-field condenser lens (N.A. 0.8–0.95).

2.3 Photocatalytic water reduction reaction

Cellulose (powder through 38 μm mesh) and wood pellets used for photocatalytic H_2 production experiments were purchased from FUJIFILM Wako Chemical Corp. and Iwakuni Reproducing Energy Co. Ltd., respectively. Under dark conditions, an aqueous solution containing TEMPO, N-methyl imidazole (50 mM), 0.1 M substrate (glycerol or cellulose) and **DDSP-n** nanoparticles (100 μM of the Ru(II) dye) was placed in a homemade Schlenk flask-equipped quartz cell (volume: 240 or 140 mL) with a small magnetic stirring bar. For the reaction with **PRCC-n** paper, the **DDSP-n** dispersion and substrate were replaced by the **PRCC-n** paper and the magnetic stirring bar was removed. Each sample flask was doubly sealed with rubber septa. This mixed solution was deoxygenated by Ar bubbling for 1 h. The flask was then irradiated from the side and bottom with two 18W blue LED lamps ($\lambda = 467 \pm 30$ nm; 550 mW; HepatoChem Ltd, HCK1012-01-32). The temperature was controlled at 293 K using an air circulating system (HepatoChem Ltd, HCK1006-01-023). The gas sample (1.0 mL) for each analysis was collected from the headspace using a gastight syringe (Valco Instruments Co. Inc.) equipped with an automatic pipette dispenser (Hamilton Microlab 600) and the amount of evolved H_2 was determined using a gas chromatograph (Agilent 990 Micro Gas Chromatograph). The turnover number and turnover frequency per Ru dye (PS TON and PS TOF) were estimated from the amount of evolved H_2; two photoredox cycles of the Ru(II) PS are required to produce one H_2 molecule. Each photocatalytic H_2 evolution reaction was conducted under the same conditions three times, and the average value with standard deviation is

reported. The detection limit of this gas chromatography analysis for H_2 gas was 0.05 μmol. The AQY was calculated using the following equation:

$$AQY = N_e/N_p = 2N_{H_2}/N_p$$

Here, N_e represents the number of reacted electrons, N_{H2} is the number of evolved H_2 molecules, and N_p is the number of incident photons.

2.4 Machine learning method

A Random Forest Regression (RFR) model implemented within Scikit-learn is used to calculate feature importance.[59] The number of trees is set to 100, and the random seed is fixed to ensure reproducibility. Four independent RFR models are constructed, each corresponding to one of the following objective variables: iAQY(%) and PS TOF for 24 h of reaction in 0.1 M glycerol aqueous solution and 0.1 M cellulose aqueous dispersion, respectively. Fifteen variables as listed in Table S2, Pt cocatalyst loading (*Pt loaded*), Ru(II) dye concentrations in the immobilization reactions (*RuP6* and *RuCP6 conc*), immobilization order of Ru(II) dyes (*RuP6* and *RuCP6 order*), reaction times for Ru(II) dye immobilization (*RuP6* and *RuCP6 time*), Ru(II) dye loading (*RuP6* and *RuCP6 loaded*), the MCl_2O_4 salt concentration for M^{4+} immobilization (MCl_2O_4*conc*, M = Zr, Hf), reaction time for M^{4+} immobilization (*M time*), the total amount of immobilized Ru(II) dyes (*sum RuP6 + RuCP6*), and the molar ratio of immobilized Ru(II) dyes (*RuP6/RuCP6 ratio*), are used as descriptor variables. In a similar manner, the Pearson correlation coefficient is calculated for the 15 descriptor variables and the 4 objective variables to evaluate their linear relationships.

3 Results and discussion

3.1 Characterization of DDSP-n

Twelve different **DDSP-n** were assembled according to our previously reported synthetic procedure (Scheme 1),[53] whereby the concentration of the inner **RuP6** dye (A mM), Zr^{4+} cation binder (B mM), outer **RuCP6** dye (C mM), and Hf^{4+} surface-capping cation (D mM) were varied to elucidate the effects of the following factors on the photocatalytic activity (Table 1 and the Experimental section in the SI): immobilization order of Ru(II) dyes (**n = 0n** and **0r**); the inner **RuP6** dye concentration (**n = 1a** and **1b**); the Zr^{4+} concentration (**n = 2a** and **2b**); the outer **RuCP6** dye concentration (**n = 3a** and **3b**); the relationship between Zr^{4+} and **RuCP6** (**n = 4a** and **4b**); and the Hf^{4+} concentration (**n = 5a** and **5b**). The dye loading amounts were estimated based on the UV-vis absorption spectra of the supernatant solution following dye immobilization (Fig. S1–S6) and further confirmed using XRF spectra of **DDSP-n** in the solid state.

The estimated amounts of **RuP6** and **RuCP6** dyes loaded onto the Pt-TiO₂ surfaces are listed in Table 1. When the immobilization order of **RuP6** and **RuCP6** was reversed to drastically alter the dual-dye layer structure (Hf^{4+}-**RuCP6**-Zr^{4+}-**RuP6**@Pt-TiO₂ for **n = 0n** and Hf^{4+}-**RuP6**-Zr^{4+}-**RuCP6**@Pt-TiO₂ for **n = 0r**), the loaded amount of **RuP6** immobilized directly on the TiO₂

Table 1 Relationship between the DDSP-n synthetic conditions and amounts of loaded Ru(II) dyes

n	Pt (wt%)	A: RuP^6 conc. (mM)	B: Zr^{4+} conc. (mM)	C: RuCP^6 conc. (mM)	D: Hf^{4+} conc. (mM)	Loaded RuP^6 (nmol mg^{-1})	RuP^6 footprint (nm^2)	Loaded RuCP^6 (nmol mg^{-1})	RuCP^6 footprint (nm^2)
0n	1.38	2.676	20	2.779	20	373.4	0.978	286.8	1.27
0r	1.38	2.626^a	20	2.967^a	20	355.0	1.03	314.9	1.16
1a	1.34	2.799	20	2.776	20	407.4	0.896	191.1	1.91
1b	1.34	0.6403	20	2.776	20	122.7	2.97	230.2	1.59
2a	1.34	2.679	40	2.735	20	366.0	0.997	254.5	1.43
2b	1.34	2.679	0	2.735	20	374.5	0.975	34.9	10.5
3a	1.34	2.863	40	3.479	20	190.5	1.92	483.5	0.755
3b	1.34	2.863	40	2.305	20	185.7	1.97	269.9	1.35
4a	1.34	2.747	120	1.443	20	377.7	0.967	191.9	1.90
4b	1.34	2.747	20	1.443	20	381.8	0.956	192.3	1.90
5a	1.38	2.746	120	1.447	20	392.8	0.929	238.3	1.53
5b	1.38	2.746	120	1.447	120	396.3	0.921	219.7	1.66

^{a} RuP^6 and RuCP^6 were immobilized in reverse order.

surface of **DDSP-0n** was found to be ~20% larger than that of **RuCP^6** on **DDSP-0r**. This is reasonable because the molecular size of **RuP^6** is smaller than that of **RuCP^6**, owing to the lack of a methylene spacer between the bipyridine ring and the phosphonate group. The **RuP^6** and **RuCP^6** molecular footprints, estimated based on their loaded amounts (373.4 and 314.9 nmol mg^{-1}) and the surface area of TiO$_2$ nanoparticles (~2197 cm^2 mg^{-1}), were 0.978 and 1.16 nm^2, respectively, which was consistent with the estimation based on their molecular size (~1 nm). Thus, the TiO$_2$ nanoparticle surface was almost entirely encapsulated by the initially immobilized dye molecules (**RuP^6** for **DDSP-0n** and **RuCP^6** for **DDSP-0r**). As a result, the subsequently immobilized dye (**RuCP^6** for **DDSP-0n** and **RuP^6** for **DDSP-0r**) was not directly bonded to the TiO$_2$ surface but immobilized *via* Zr^{4+}–PO$_3{}^{2-}$ coordination bonds to form a second dye layer on the outer surface of the first dye layer.

When the **RuP^6** dye concentration was reduced four-fold from 2.8 mM ($n = $ **1a**) to 0.64 mM ($n = $ **1b**), the loaded amount of **RuP^6** decreased by approximately 75%. Considering that for **DDSP-1b**, the ultracentrifugation supernatant obtained after **RuP^6** immobilization was almost colorless (Fig. S2b) and the amount of **RuP^6** was insufficient to fully cover the TiO$_2$ nanoparticle surface. This resulted in a significantly enlarged **RuP^6** footprint (2.96 nm^2) that was three-fold larger than the molecular size. Thus, the TiO$_2$ nanoparticle surface in **DDSP-1b** is thought to be covered by not only the initially immobilized **RuP^6** but also the subsequently introduced **RuCP^6**.

Doubling the Zr^{4+} cation concentration to 40 mM ($n = $ **2a**) was found to have a minimal effect on the **RuCP^6** loading ($n = $ **2a** and **2b**), likely because the original concentration of 20 mM, which corresponds to 2 eq. of Zr^{4+} cations per free phosphonate group of **RuP^6**, was sufficient to fully load the Zr^{4+} cations onto all the free phosphonate groups of **RuP^6**. In contrast, in the absence of Zr^{4+} (0 mM, $n = $ **2b**), the amount of immobilized **RuCP^6** was drastically reduced by ~85% compared to that in **DDSP-2a**. This indicated that the Zr^{4+} cations bound by the phosphonate groups of the initially immobilized **RuP^6** moieties were necessary for the stable immobilization of the **RuCP^6** outer dye layer. The XRF spectra of the **DDSP-n** samples shown in Fig. 1 clearly indicate the absence of Zr Kα and Kβ radiation in the **DDSP-2b** spectrum only. This was supported by the XRF spectra of the **DDSP-n** samples shown in Fig. 1: compared to the Ru Kα radiation intensities of the other **DDSP-n** samples, that of **DDSP-2b** is observably lower due to the absence of Zr, as confirmed by the lack of Zr Kα and Kβ radiation in its spectrum. In contrast, the loading amount of **RuCP^6** increased with the increasing **RuCP^6** dye concentration ($n = $ **3a**). Considering the relatively smaller footprint of **RuCP^6** in **DDSP-3a** (<1 nm^2), it is possible that after forming an initial molecular layer on the surface of the **RuP^6** inner layer through Zr^{4+}-phosphonate bonding, **RuCP^6** formed an additional second layer *via* hydrogen bonding interactions with the phosphonate groups of the existing **RuCP^6** outer layer. Conversely, when the **RuCP^6** concentration was halved (~1.4 mM, $n = $ **4a** and **4b**), the amount of loaded **RuCP^6** decreased by approximately 40%, even when the Zr^{4+} concentration was increased to 120 mM ($n = $ **4a**). Considering that the Zr K radiation observed for **DDSP-4a** was
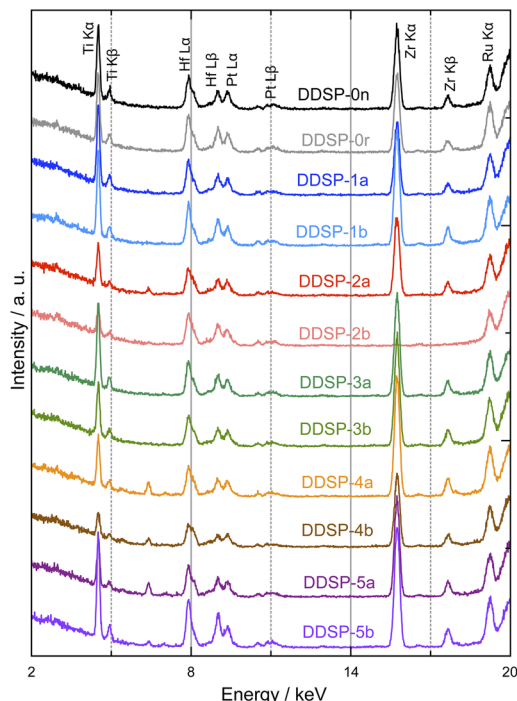
Fig. 1 XRF spectra of the DDSP-*n* samples in the solid state obtained at 293 K.

~1.7-fold higher than that for **DDSP-4b** (Fig. 1), Zr^{4+} cation absorption in the former possibly occurs not only *via* coordination with the phosphonate groups of **RuP**[6] but also through

the formation of Zr-oxide/hydroxide on the outer surface of the inner **RuP**[6] dye layer. As expected, the Hf^{4+} cation concentration had a negligible effect on the **RuP**[6] and **RuCP**[6] loading amounts (*n* = **5a** and **5b**) because the Hf^{4+} cations were added after the formation of the dual-dye-layer structure (**RuCP**[6]-Zr^{4+}-**RuP**[6]@Pt-TiO_2) on the Pt-TiO_2 nanoparticle surface. Notably, Fig. 1 shows that the Hf L radiation intensities were the highest for **DDSP-5b**, which was the only sample fabricated under increased Hf^{4+} concentration conditions (120 mM). Considering that all 12 **DDSP-*n*** samples gave rise to comparable Pt L radiation (9.4 keV, adjacent to Hf Lβ radiation) intensities, the loading amount of Hf^{4+} cations in **DDSP-5b** is expected to be higher than that in **DDSP-5a**, likely due to the formation of Hf-oxide/hydroxide on the outer surface of the **RuCP**[6] dye layer.

3.2 Emission spectra of DDSP-*n*

Emission spectra of all 12 **DDSP-*n*** were obtained in aqueous dispersions to verify that electron transfer quenching of emissive Ru(II) dyes occurred upon immobilization onto the TiO_2 nanoparticles (Fig. 2). The intensities of the emissions derived from the [3]MLCT phosphorescence of the Ru(II) dyes in the **DDSP-*n*** samples were approximately 18- to 180-fold weaker than those of **RuP**[6] and **RuCP**[6] in aqueous solution (Fig. 2b), even at equal Ru(II) dye concentrations ([Ru] = 30 μM). The marked difference in emission between the immobilized and free Ru(II) dyes indicates effective electron transfer quenching by the TiO_2 nanoparticles, as discussed in numerous studies.[60] Interestingly, from the emission spectra of the 12 **DDSP-*n*** samples shown in Fig. 2a, it is evident that the emission maximum of
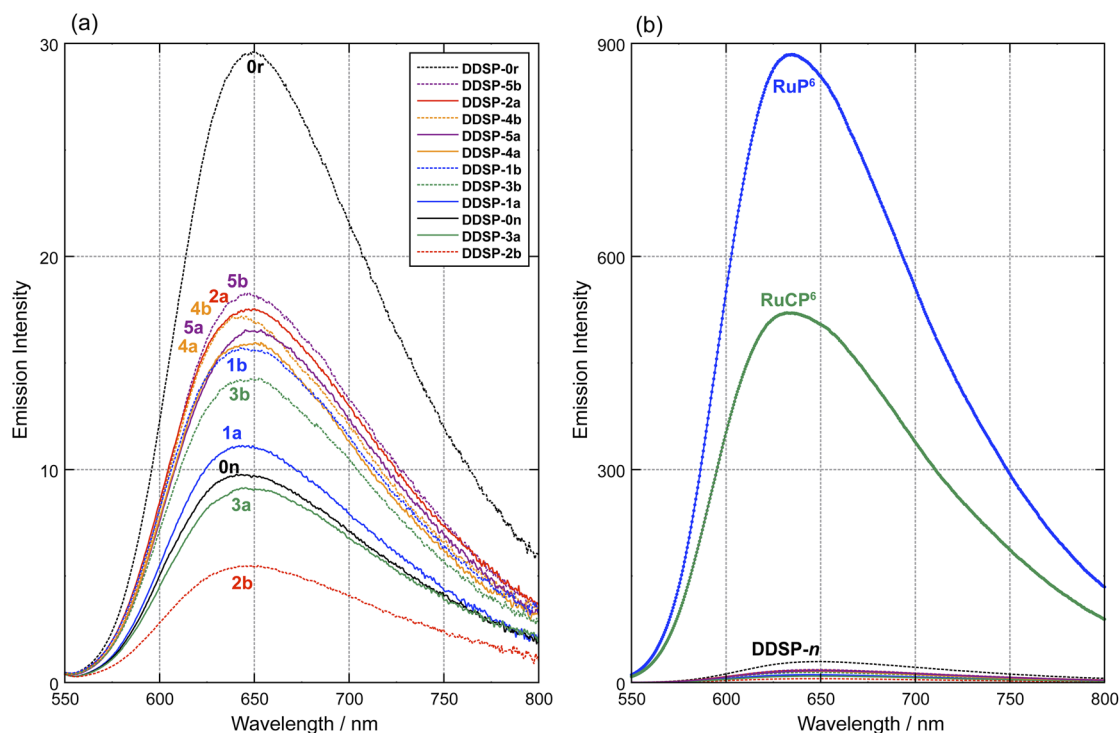

Fig. 2 (a) Emission spectra of **DDSP-*n*** (*n* = **0n**-**5b**) aqueous dispersions ([Ru] = 30 μM, λ_{ex} = 460 nm), and (b) plotted together with the emission spectra of aqueous solutions of **RuP**[6] (blue) and **RuCP**[6] (green). All samples were degassed by Ar bubbling for 20 min and spectra were obtained at 293 K.

DDSP-0r is red-shifted and substantially higher (I = 29.6 at 650 nm) compared with those of the other **DDSP-n** (I < 18.3 at approximately 645 nm) in spite of the comparable absorbance in the UV-vis diffuse transmission spectra of **DDSP-n** aqueous dispersions (Fig. S7). Considering that the emission maximum of **RuP⁶** appears at a slightly longer wavelength (∼3 nm) than that of **RuCP⁶** in aqueous solution due to the lack of an electron-donating methylene spacer between the bipyridine ring and phosphonate group, the stronger and slightly red-shifted emission of **DDSP-0r** is assignable to ³MLCT phosphorescence from the outer **RuP⁶** dye in the dual-dye layer.

This hypothesis is supported by previously reported findings,[50] which suggest that energy transfer from photoexcited **RuCP⁶*** to **RuP⁶** occurs rapidly when these two dyes are in close proximity to each other. Although energy transfer from **RuCP⁶*** to **RuP⁶** presumably occurs in all **DDSP-n**, in **DDSP-n** (n ≠ 0r), **RuP⁶** was directly immobilized on the TiO₂ surface, enabling the rapid injection of the photoexcited electron from the resultant **RuP⁶*** species into the TiO₂ nanoparticle (electron transfer quenching), resulting in suppressed **RuP⁶** emissions. On the other hand, in the case of **DDSP-0r**, **RuP⁶** was immobilized as the outer layer on the surface of the **RuCP⁶** inner layer, leading to lower-efficiency electron transfer quenching and, consequently, enhanced **RuP⁶** emission.

3.3 Photocatalytic H₂ production with glycerol/cellulose oxidation

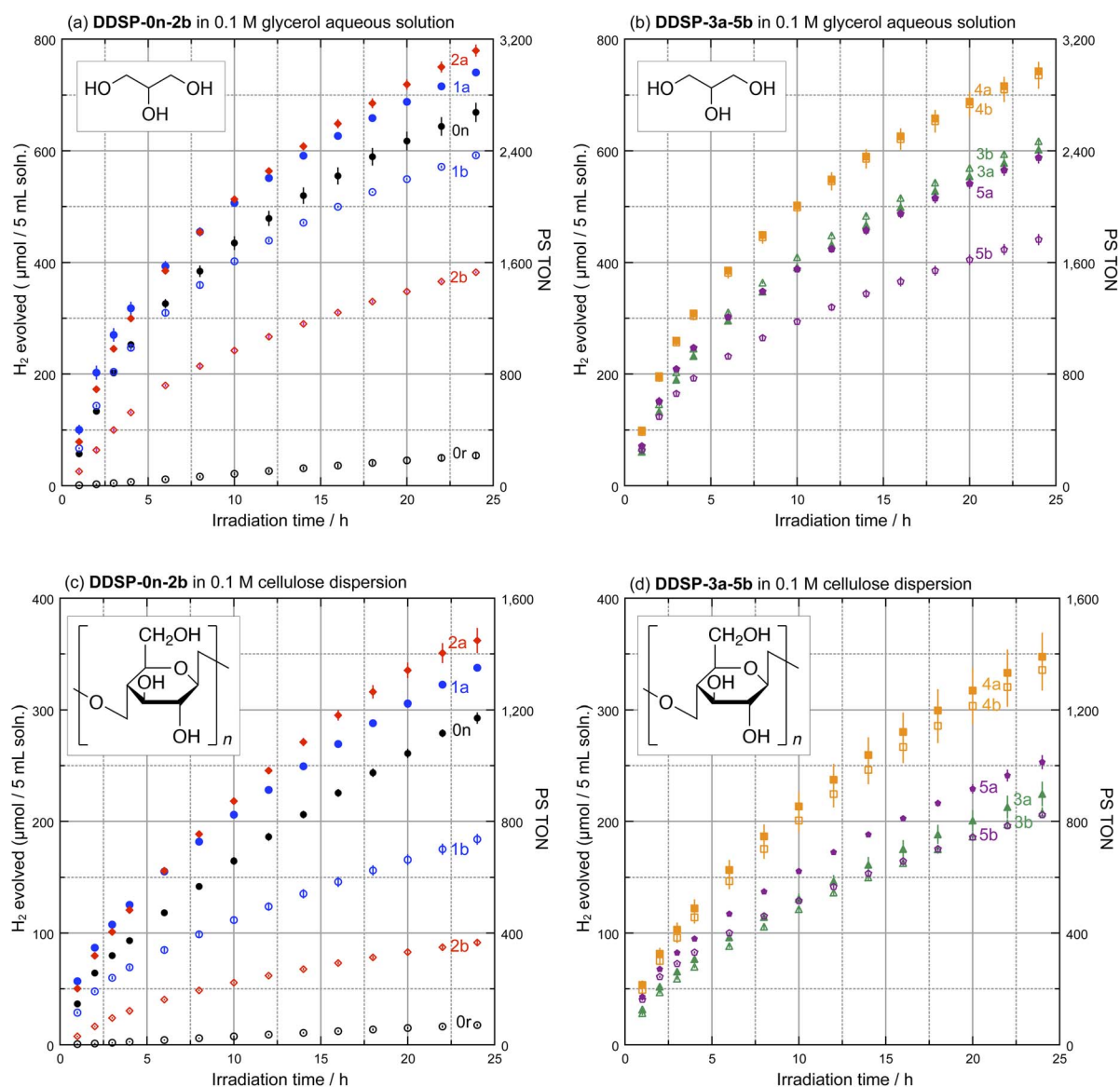To evaluate the relationship between the various structural parameters of **DDSP-n** and the photocatalytic activity,

Fig. 3 Photocatalytic H₂ production using **PRCCs** comprising various **DDSP-n** conducted under blue-light irradiation (λ = 467 ± 30 nm; 550 mW) in (a and b) 0.1 M glycerol aqueous solution or (c and d) 0.1 M cellulose aqueous dispersion (initial pH = 9); [TEMPO] = 15 mM, [NMI] = 50 mM; the concentration of the Ru(ɪɪ) photosensitizer was adjusted to 100 µM for all reactions.
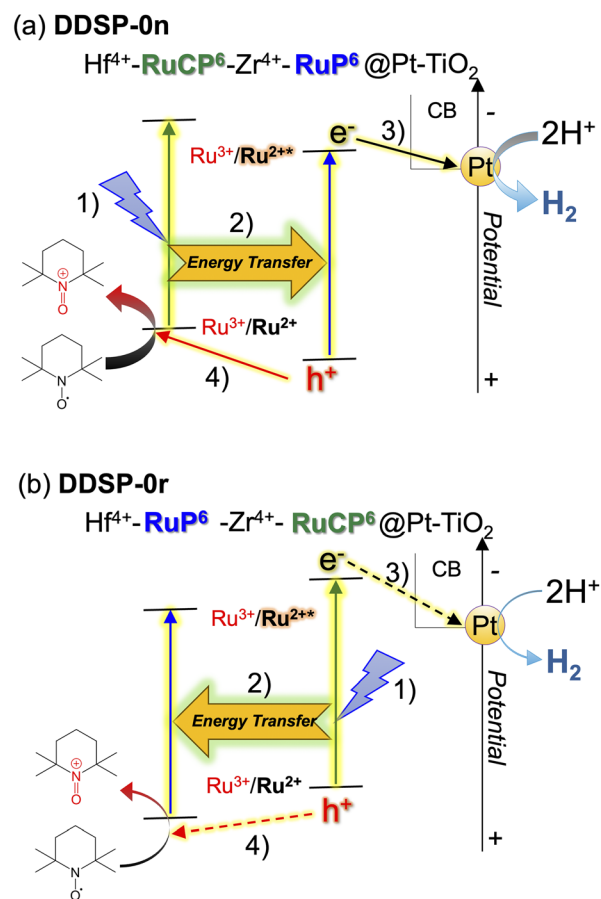
Table 2 Photocatalytic H$_2$ production *via* PRCC comprising various **DDSP-*n*** and 15 mM TEMPO in a 0.1 M glycerol aqueous solution or 0.1 M cellulose aqueous dispersion[a]

n	0.1 M glycerol solution				0.1 M cellulose dispersion			
	Evolved H$_2$ (μmol)	PS TON	PS TOF	*i*AQY (%)	Evolved H$_2$ (μmol)	PS TON	PS TOF	*i*AQY (%)
0n	669.0 ± 16.0	2676	111.5	1.48	292.7 ± 4.52	1171	48.78	0.943
0r	54.3 ± 4.53	217	9.04	0.021	17.7 ± 0.62	70.8	2.95	0.016
1a	740.0 ± 2.37	2960	123.3	2.59	337.5 ± 2.46	1350	56.26	1.47
1b	591.9 ± 1.89	2368	98.65	1.73	183.9 ± 4.33	735.5	30.64	0.742
2a	779.3 ± 9.65	3117	129.9	2.04	362.0 ± 10.7	1447	60.33	1.30
2b	382.5 ± 0.68	1530	63.76	0.662	91.5 ± 1.32	366.0	15.25	0.197
3a	602.0 ± 14.5	2408	100.3	1.57	224.6 ± 10.5	898.2	37.43	0.817
3b	617.2 ± 4.50	2468	102.9	1.77	207.7 ± 4.36	830.8	34.62	0.733
4a	742.1 ± 6.26	2968	123.7	2.56	347.4 ± 21.0	1390	57.91	1.38
4b	735.0 ± 23.1	2940	122.5	2.50	335.5 ± 17.8	1342	55.92	1.27
5a	587.6 ± 9.31	2351	97.94	1.84	253.1 ± 5.74	1012	42.19	1.11
5b	440.7 ± 8.92	1762	73.44	1.65	205.8 ± 0.19	823.0	34.29	1.04

[a] [a]Reaction conditions: [PS] = 100 μM in total, [TEMPO] = 15 mM, [NMI] = 50 mM aqueous solution (pH 9), λ_{ex} = 467 ± 30 nm (550 mW). The reaction solution was purged by bubbling Ar for 1 h prior to light irradiation. Numerical values represent the average of at least three experiments. Definitions: PS, photosensitizer; TON, turnover number over 24 h of reaction; TOF, turnover frequency over 24 h of reaction; *i*AQY, apparent quantum yield during the initial 1 h of reaction.

photocatalytic H$_2$ production was investigated using the fabricated **DDSP-*n***s in combination with TEMPO-catalyzed glycerol/cellulose oxidation under the following reaction conditions: [Ru] = 100 μM, [TEMPO] = 15 mM, [NMI] = 50 mM, and [glycerol or cellulose] = 0.1 M in aqueous media under blue LED light irradiation (λ = 467 ± 30 nm, 550 mW). Fig. 3(a–d) show the photocatalytic H$_2$ production attained in 0.1 M aqueous glycerol and aqueous cellulose dispersion, respectively. The estimated amounts of H$_2$ evolved, turnover numbers, and turnover frequencies achieved per unit of Ru(II) photosensitizer (PS TONs and TOFs) during 24 h of reaction and the apparent quantum yield for the initial 1 h of reaction (*i*AQY) are listed in Table 2. For both reactions, significant differences were observed for the amount of evolved H$_2$ among the 12 **DDSP-*n*** series, indicating that how to synthesize **DDSPs** is crucial for the photocatalytic activity of the PRCC system. In the following five subsections, we discuss the relationship between the photocatalytic H$_2$ production activity and the **DDSP** preparation parameters in detail based on our previously suggested mechanism (see Scheme S1 in the SI).

3.3.1 Importance of Ru(II) dye immobilization order. The standard **DDSP-0n** sample synthesized according to our previously published procedure[53] produced 669.0 and 292.7 μmol of H$_2$ after 24 h of photocatalysis in aqueous glycerol and cellulose media, respectively, under blue light irradiation (Fig. 3(a) and (c)). **DDSP-0r**, fabricated using an analogous procedure but with the reversed order of dye immobilization, produced an order of magnitude less H$_2$ (54.3 and 17.7 μmol in glycerol and cellulose, respectively) than **DDSP-0n** in both media. Moreover, the apparent quantum yields attained using these two catalysts in the initial 1 h (*i*AQY) of the photocatalytic reaction also differed substantially; the estimated *i*AQY of **DDSP-0n** (1.48% and 0.943%) obtained in 0.1 M aqueous glycerol and cellulose media was 70- and 58-fold larger than the corresponding values for **DDSP-0r** (0.021 and 0.016%). These contrasting results clearly

(a) DDSP-0n

Hf^{4+}-**RuCP^6**-Zr^{4+}-**RuP^6**@Pt-TiO$_2$

(b) DDSP-0r

Hf^{4+}-**RuP^6**-Zr^{4+}-**RuCP^6**@Pt-TiO$_2$

Scheme 2 Schematic energy diagrams of the redox cascade structures of (a) *DDSP-0n* = Hf^{4+}-RuCP^6-Zr^{4+}-RuP^6@Pt-TiO$_2$ and (b) **DDSP-0r** = Hf^{4+}-RuP^6-Zr^{4+}-RuCP^6@Pt-TiO$_2$. The charge separation mechanism in DDSP-0n is proposed as follows: (1) photoexcitation of outer RuCP^6, (2) energy transfer to (or direct photoexcitation of) inner RuP^6, (3) electron injection to TiO$_2$, and (4) hole migration from inner RuP^6 to outer RuCP^6, followed by hole donation to the TEMPO• radical mediator.

show that the order of Ru(II) dye immobilization during the synthesis of **DDSP-n** is a crucial factor affecting the photocatalytic activity of the **DDSP-n** series. This outcome is logical under the reasonable assumption that the photoinduced charge-separation mechanism in **DDSP-n** is governed by the proposed photoredox cascade structure of the dual-dye layer (Scheme 2). The hole generated as a result of photoexcited electron injection into TiO_2 from the inner **RuP⁶** dye of **DDSP-0n** readily migrates to the outer **RuCP⁶** dye, facilitated by a sufficiently large and positive redox potential difference between these two dyes (process 4 in Scheme 2a). Conversely, hole migration in **DDSP-0r** from the inner **RuCP⁶** dye to the outer **RuP⁶** dye is thermodynamically unfavorable because the redox potential difference between these two dyes becomes negative when their positions are switched (process 4 in Scheme 2b). Furthermore, as discussed above, the reversal of the energy transfer direction in **DDSP-0r** is expected to negatively affect the photocatalytic activity. In other words, in the case of **DDSP-0r**, electron injection from the photoexcited **RuCP⁶*** dye to the TiO_2 core competes with the transfer of excitation energy to the outer **RuP⁶** dye (processes 2 and 3 in Scheme 2b).

3.3.2 Effect of loading amount of inner RuP⁶.

DDSP-1a, containing a lower amount of Pt-cocatalyst, produced 10–15% more H_2 (Fig. 3a and c, 740.0 and 337.5 μmol in glycerol solution and cellulose dispersion, respectively) than **DDSP-0n**, suggesting the importance of the loading amount and size of the Pt-cocatalyst on the TiO_2 nanoparticle surface, as discussed in our previous paper.[60] In contrast, **DDSP-1b**, containing a three-fold lower **RuP⁶** loading than **DDSP-0n**, generated approximately 10% and 40% less H_2 than **DDSP-0n** after 24 h of photocatalytic reaction in 0.1 M glycerol solution and cellulose dispersion, respectively. The lower activity of **DDSP-1b** than **DDSP-0n** likely resulted from charge recombination in the **RuCP⁶** dyes directly immobilized on the TiO_2 surface. As discussed in the "3.1 Characterization of **DDSP-n**" section, the TiO_2 nanoparticle surfaces of **DDSP-0n** and -**1a** were fully covered by **RuP⁶**, whereas partial coverage of the TiO_2 surface was observed for **DDSP-1b** after **RuP⁶** loading due to the lower concentration of dye solution used. This would allow for the direct immobilization of the **RuCP⁶** dye on the TiO_2 surface in the subsequent step; in this scenario, the hole generated after electron injection from the inner **RuP⁶**(h⁺) dye can migrate to **RuCP⁶**, which would induce rapid charge recombination between electron-injected TiO_2 and one-electron oxidized **RuCP⁶**(h⁺) due to their direct contact. Therefore, to suppress such recombination, the TiO_2 surface should be fully encased by the **RuP⁶** dye layer, as in the cases of **DDSP-0n** and -**1a**.

3.3.3 Importance of Zr⁴⁺ loading.

DDSP-2a and -**2b** were synthesized using 40 and 0 mM Zr^{4+} salt concentrations, respectively, to evaluate the effects of the Zr^{4+} cation binder on dual-dye layer formation in **DDSP-2n** and, in turn, on its activity (Table 1). **DDSP-2a** produced the largest amount of H_2 in both glycerol solution and cellulose dispersion (Fig. 3a and c, 779.3 and 362.0 μmol, respectively) among the 12 **DDSP-n** samples. In contrast, **DDSP-2b**, fabricated in the absence of Zr^{4+} salt, generated significantly less H_2 in both glycerol solution and cellulose dispersion (382.5 and 91.5 μmol, respectively).

Considering that **RuCP⁶** dye loading in **DDSP-2b** was only 14% that of **DDSP-2a**, this marked difference between their photocatalytic activities suggests the importance of **RuCP⁶** loading (outer layer) in photocatalytic activity. As discussed above (see Scheme 2), the outer **RuCP⁶** dye in **DDSP-n** ($n \neq 0r$) serves to accept the hole from the photo-induced electron-injected **RuP⁶**(h⁺) dye. Thus, **DDSP-2a** displayed considerably higher activity than **DDSP-2b** primarily because the charge recombination between the electron-injected TiO_2 surface and one-electron oxidized directly immobilized **RuP⁶**(h⁺) was effectively suppressed by enabling hole migration from **RuP⁶**(h⁺) to the outer **RuCP⁶** via Zr^{4+}-phosphonate coordination bonds.

3.3.4 Effect of loading amount of outer RuCP⁶.

The **RuCP⁶** dye concentration used to fabricate **DDSP-3a** was 1.5-fold higher than that used for **DDSP-3b** (Table 1). Higher **RuCP⁶** loading may potentially lead to enhanced photoinduced charge-separation efficiency, primarily because of facilitated hole migration from the electron-injected one-electron oxidized **RuP⁶**(h⁺) to the outer **RuCP⁶** dye. However, the amounts of H_2 evolved using **DDSP-3a** and -**3b** after 24 h of reaction did not differ significantly in both glycerol solution (Fig. 3b, 602.0 and 617.2 μmol, respectively) and cellulose dispersion (Fig. 3d, 224.6 and 207.7 μmol, respectively). In contrast, the low **RuCP⁶** loading in **DDSP-2b** resulted in substantially lower activity, suggesting that the outer **RuCP⁶** dye is important for facilitating charge separation; however, higher **RuCP⁶** loadings do not necessarily lead to higher activity. To further clarify the effect of **RuCP⁶** loading on the photocatalytic H_2 production performance, the **RuCP⁶** loading was reduced and the resultant **DDSP-4a** and -**4b** catalysts were evaluated under the same reaction conditions. Surprisingly, despite the reduced **RuCP⁶** loading, both **DDSPs** produced large amounts of H_2 in both glycerol solution (Fig. 3b, 742.1 and 735.0 μmol) and cellulose dispersion (Fig. 3d, 347.4 and 335.5 μmol). Importantly, the amounts of generated H_2 were comparable to those produced using **DDSP-2a**, which displayed the best performance among the 12 **DDSP-n** samples. Notably, the activities of **DDSP-4a** and -**4b** were comparable to those of **DDSP-1a**, which contained higher **RuCP⁶** dye loading than **DDSP-4**. Thus, excessive loading of **RuCP⁶** on the outer surface of the **RuP⁶** inner layer does not necessarily lead to improved photocatalytic activity. Although the reason for this is currently under investigation, one plausible explanation is that lateral hole hopping, which has been discussed as a possible origin of charge recombination,[61] may be suppressed by reducing the **RuCP⁶** loading.

3.3.5 Effect of loading amount of surface Hf⁴⁺ cations.

DDSP-5a and -**5b** were synthesized using 20 and 120 mM Hf^{4+} concentrations, respectively, to evaluate the effect of Hf^{4+} cation loading on the photocatalytic H_2 production performance. The amounts of H_2 evolved after 24 h of photocatalytic reaction using **DDSP-5b** in glycerol solution and cellulose dispersion (Fig. 3b and d, 440.7 and 205.8 μmol) were approximately 20% lower than those produced using **DDSP-5a** (587.6 and 253.1 μmol). Considering that both **DDSP-5** catalysts comprise the same dual-dye-layer structure on the Pt-TiO_2 nanoparticle surface (Hf^{4+}-**RuCP⁶**-Zr^{4+}-**RuP⁶**@Pt-TiO_2) and comparable **RuCP⁶** and **RuP⁶** loadings, the activity difference between **DDSP-**

5a and **-5b** was inferred not to originate from the photoinduced charge-separation process in the dual-dye layer structure but from the loading amount of Hf⁴⁺ cations on the **DDSP** surface. As discussed above, the XRF spectra of **DDSP-5b** and **-5a** (Fig. 1) indicated thicker Hf⁴⁺oxide/hydroxide layer formation in the former. The thicker Hf⁴⁺ layer of **DDSP-5b** possibly hinders electron transfer from the TEMPO• radical molecule to the one-electron oxidized **RuCP⁶**(h⁺) on the outer surface of the **DDSP** nanoparticles, leading to decreased photocatalytic activity.

3.4 Machine learning study to assess the importance of DDSP-*n* structural parameters

As discussed above, the photocatalytic activity of our PRCC system is affected to varying degrees by numerous structural and synthetic parameters; thus, a random forest regression model within supervised machine learning was implemented to unveil the salient features for designing highly active **DDSP-*n***. As **PRCC** system features, we selected the 15 parameters, directly obtained from the synthesis of **DDSP-*n*** (see Table S2 for details). The concentrations of TEMPO, NMI, and the substrate (glycerol or cellulose) were omitted from the list because their concentrations were kept constant in all reactions listed in

Table 2 ([TEMPO] = 15 mM, [NMI] = 50 mM, [substrate] = 0.1 M). Feature importance results for the *i*AQY of **DDSP-*n*** in 0.1 M glycerol and cellulose are shown in Fig. 4a and b, respectively. For both reaction conditions, the immobilization order of **RuP⁶** (="*RuP6 order*") was suggested as the most or second most important feature. This is consistent with the significantly different activities of the **DDSP-0** series, as discussed above (see the "*3.3.1 Importance of Ru(ii) dye immobilization order*" section). A striking difference between the two reaction conditions was found to be the importance of the "*RuP6 loaded*" feature, suggested to be the most important feature for photocatalysis in 0.1 M cellulose dispersion, whereas it was ranked 7th in 0.1 M glycerol solution. The higher importance of **RuP⁶** loading in 0.1 M cellulose dispersions can be interpreted as the possibility of **RuCP⁶** binding directly to TiO₂ and acting as the charge recombination center being higher in water-insoluble cellulose dispersions with a slower TEMPO oxidation catalytic cycle than in water-soluble glycerol solution, as observed for the **DDSP-1** series (see the "*3.3.2. Effect of loading amount of inner **RuP⁶**"* section). The importance of features related to Zr⁴⁺ and Hf⁴⁺ cations are contrasting and features related to Zr⁴⁺ ions had significant values, whereas those related to Hf⁴⁺ ions were
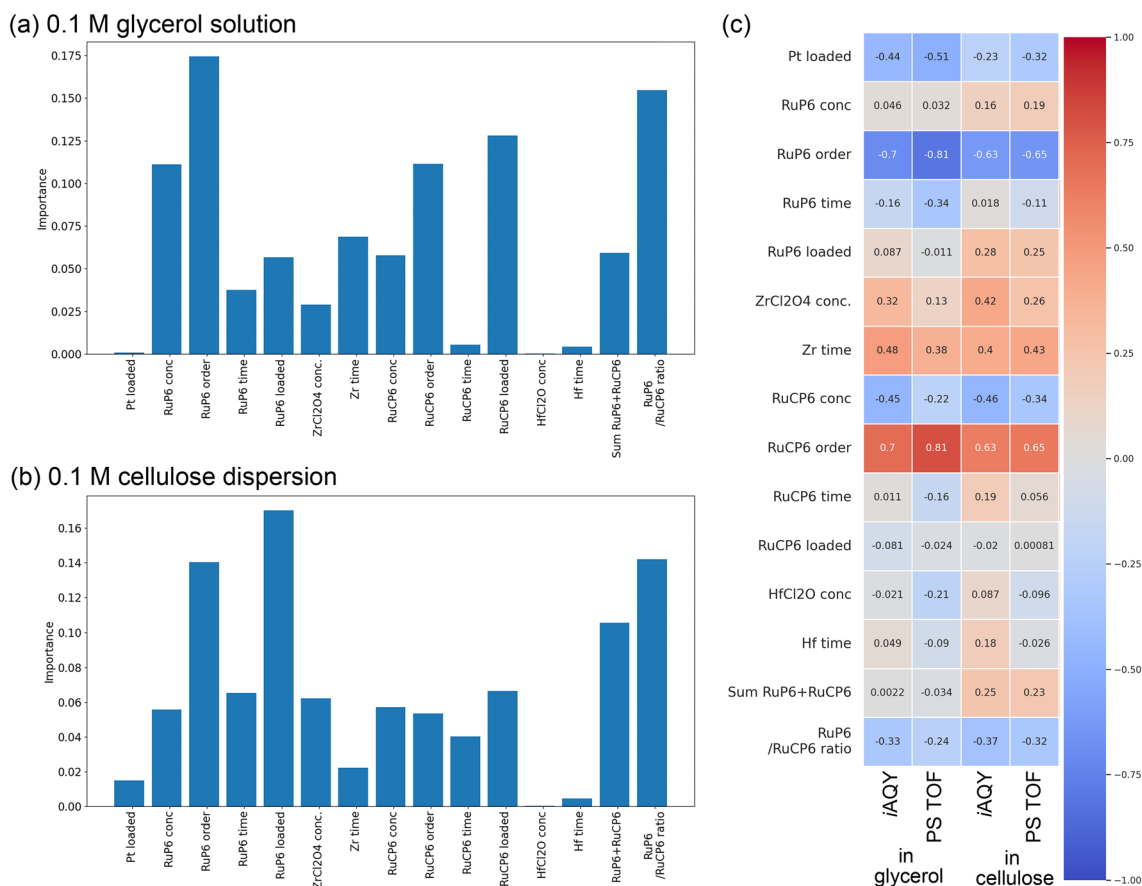

Fig. 4 Feature importance calculated using random forest regression for apparent quantum yield of the initial 1 h of reaction (*i*AQY) using the **DDSP-*n*** series in the presence of 15 mM TEMPO, 50 mM NMI and (a) 0.1 M glycerol aqueous solution, or (b) 0.1 M cellulose aqueous dispersion. (c) Pearson correlation coefficient matrix heat map of the feature set for photocatalytic H₂ production activities (*i*AQY and PS TOF) in 0.1 M glycerol solution and cellulose dispersion.

almost zero. This trend is interpreted to arise due to the distinct roles of these M^{4+} cations: the inner Zr^{4+} cations act as a binder in the formation of the dual-dye-layer structure on the $Pt-TiO_2$ nanoparticle surface, whereas the outer Hf^{4+} cations only stabilize the layered structure by forming $Hf^{4+}-PO_3$ coordination bonds on the outer surface of **DDSP-n** nanoparticles.

We further analysed the relationship between the 15 features and photocatalytic activity using a Pearson correlation coefficient heat map (Fig. 4c). The correlation coefficients further revealed the importance of the Ru(ɪɪ) dye immobilization order; the negative and positive correlation values close to −1 and +1 for the "*RuP6* and *RuCP6 order*", respectively, suggest that higher photocatalytic activity will be achieved by first immobilizing **RuP6**, followed by **RuCP6** under both reaction conditions. This is because the immobilization order is crucial for the formation of a suitable photoredox potential cascade, as observed for the **DDSP-0** series (Scheme 2a). In this regard, the positive correlation values for "*ZrCl2O4conc*" and "*Zr time*" are noteworthy. These values suggest that Zr^{4+} immobilization should be conducted at higher $ZrCl_2O_4$ concentrations over a longer time to maximize photocatalytic activity. This may reflect the higher activity of the **DDSP-4** series synthesized at higher Zr^{4+} ion concentrations. Similarly, negative correlation values were also suggested for the "*RuP6/RuCP6 ratio*" for both reaction substrates, indicating the importance of **RuCP6** outer layer formation, as suggested by the significantly dissimilar activities within the **DDSP-2** series. Significantly negative correlation values were also suggested for "*Pt loaded*". Although this feature implies that higher photocatalytic activity may be achieved by reducing the Pt cocatalyst loading on TiO_2 nanoparticles, as reported recently,[35] further experiments are needed to obtain definitive conclusions, as in this study, Pt cocatalyst loading was varied within a limited range of 1.34–1.38 wt%. The importance of the **DDSP** synthetic parameters, determined by machine-learning analysis, is summarized as follows.

(A) The **RuP6** and **RuCP6** immobilization order is crucial for generating a suitable photoredox cascade structure on the Pt-TiO_2 nanoparticle surface.

(B) The **RuP6** loading factor is more important for the photocatalytic conversion of cellulose than that of glycerol, probably because a longer lifetime of the photoinduced charge-separated state would be beneficial for the TEMPO-mediated conversion of insoluble cellulose.

(C) The loading of Zr^{4+} cations is crucial for forming a stable dual-dye-layer structure that contributes to the photoinduced charge separation on the Pt-TiO_2 nanoparticle surface.

(D) A high **RuCP6** concentration is not required for the dye immobilization reaction, implying that an optimal loading level sufficiently promotes charge separation and inhibits charge recombination.

3.5 Substrate concentration dependence

To gain a deeper understanding of the reaction mechanism, the dependence of photocatalytic H_2 production coupled with TEMPO-mediated oxidation on the glycerol/cellulose concentration was investigated using **DDSP-4**, as it displayed the best
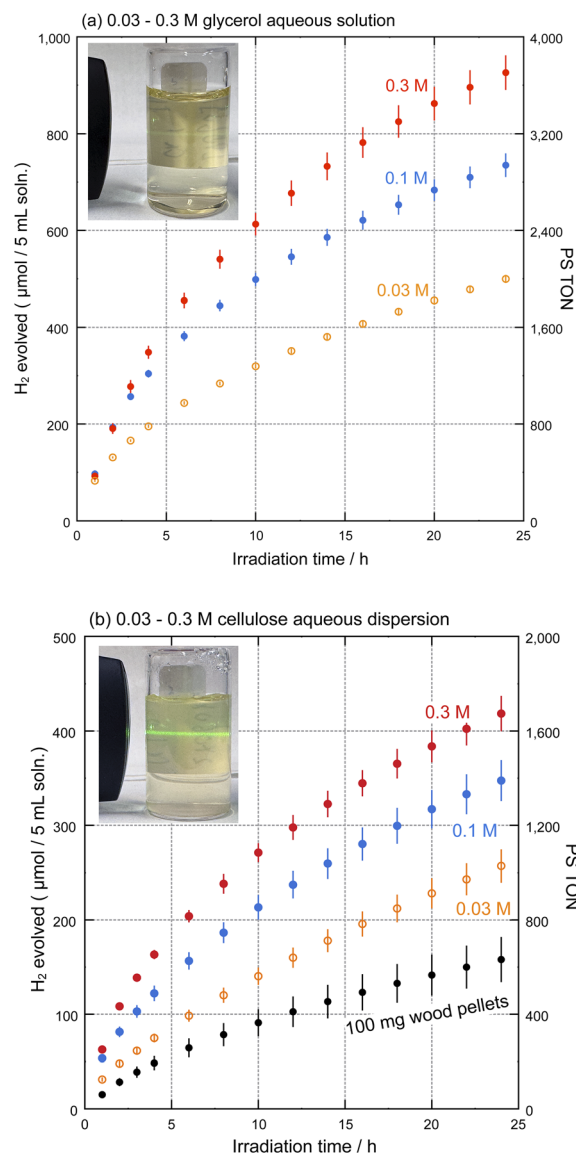

Fig. 5 Dependence of photocatalytic PRCC H_2 production on the substrate concentration for (a) **DDSP-4b** in 0.03−0.3 M glycerol aqueous solution and (b) **DDSP-4a** in 0.03−0.3 M cellulose aqueous dispersions; black circles in (b) show the results for 100 mg wood pellets instead of cellulose powder. All reactions were conducted using [TEMPO] = 15 mM and [NMI] = 50 mM, under blue-light irradiation (λ = 467 ± 30 nm; 550 mW); the Ru(ɪɪ) dye concentration of all reactions was adjusted to 100 μM (initial pH = 9). The inset photographs show Tyndall scattering of the reaction supernatants after 24 h of photocatalytic reaction in a 0.1 M substrate.

photocatalytic H_2 production performance among the 12 **DDSP-n**. Fig. 5(a) and (b) show the results of photocatalytic H_2 production using **DDSP-4b** in 0.03–0.3 M glycerol aqueous solution and **DDSP-4a** in 0.03–0.3 M aqueous dispersions of cellulose, respectively. The estimated amounts of H_2 evolved, PS TON, PS TOF during 24 h of reaction, and *i*AQY are listed in Table 3. When the glycerol and cellulose concentrations changed from 0.03 to 0.3 M, the amount of evolved H_2 and PS TON after 24 h of reaction increased markedly, by

Table 3 Results of photocatalytic H_2 production using PRCCs comprising DDSP-*n* conducted using 15 mM TEMPO, 50 mM NMI aqueous solution, and varying substrate concentrations[a]

Entry	n	Substrate	Evolved H_2 (μmol)	PS TON	PS TOF	iAQY (%)
1	**4b**	0.3 M glycerol	925.9 ± 34.5	3703	154.3	2.38
2	**4b**	0.1 M glycerol	735.0 ± 23.1	2940	122.5	2.50
3	**4b**	0.03 M glycerol	499.6 ± 7.07	1998	83.26	2.13
4	**4a**	0.3 M cellulose	418.5 ± 18.1	1674	69.74	1.62
5	**4a**	0.1 M cellulose	347.4 ± 21.0	1390	57.91	1.38
6	**4a**	0.03 M cellulose	257.0 ± 16.8	1028	42.83	0.80
7	**4a**	100 mg wood pellets	158.0 ± 23.2	632.0	26.33	0.39

[a] Reaction conditions: [PS] = 100 μM in total, [TEMPO] = 15 mM, [NMI] = 50 mM aqueous solution (pH 9), λ_{ex} = 467 ± 30 nm (550 mW). The reaction solution was purged by bubbling Ar for 1 h prior to light irradiation. Numerical values represent the average of more than three experiments. Definitions: PS, photosensitizer; TON, turnover number for 24 h of reaction; TOF, turnover frequency for 24 h of reaction; iAQY, apparent quantum yield during the initial 1 h of reaction.

approximately 85% and 63%, respectively, indicating that glycerol and cellulose acted as the electron source for H_2 production, as we previously reported.[53] Interestingly, in glycerol solution, the iAQY was negligibly dependent on the glycerol concentration (iAQY = 2.1–2.5%), whereas in cellulose dispersion, it increased two-fold from 0.80% to 1.62% when the cellulose concentration (as a monomer unit) was increased from 0.03 to 0.3 M. Considering that a higher concentration of substrate should facilitate the reduction of TEMPO$^+$ to regenerate the TEMPO$^\bullet$ radical, it can be concluded that the reduction rate of TEMPO$^+$ is sufficiently fast at 0.03 M glycerol, based on its independence on the glycerol concentration. In contrast, cellulose is a water-insoluble polymer that diffuses slower than water-soluble glycerol molecules; therefore, a 0.03 M concentration would not be sufficient for efficient TEMPO$^+$ reduction, leading to concentration-dependent behaviour in the cellulose dispersion even in the initial 1 h of reaction. The photocatalytic H_2 evolution activity gradually decreased with photoirradiation time in all six reactions, and the degree of activity decrease was more pronounced at lower glycerol and cellulose concentrations. This trend was due to a decrease in the concentration of the reaction substrates that act as electron sources for photocatalytic H_2 production using **DDSP-4** *via* the TEMPO$^\bullet$ electron mediator. Interestingly, photocatalytic H_2 production was also achieved using commercially available wood pellets instead of cellulose powder (black circles in Fig. 5b), and the estimated TON after 24 h of reaction was approximately half that in the 0.1 M cellulose dispersion (entry 7 in Table 3), which may be due to the lower dispersibility, surface area, and light shielding effect of the brown-coloured wood pellets.

The oxidation of glycerol was confirmed based on the ^{13}C NMR spectra of the reaction supernatant (Fig. 6a) obtained after ultracentrifugation of the reaction mixture to remove **DDSP-4b** nanoparticles. The two characteristic glycerol peaks at 62.6 and 72.2 ppm were barely visible after 24 h of photocatalytic reaction in 0.03 M glycerol, suggesting the complete oxidation of glycerol. This is quantitatively consistent with the PS TON of 1998 estimated from the amount of evolved H_2 (499.6 μmol); for a 300-fold concentration difference between the Ru(II) dye (100 μM = 0.1 mM) and glycerol (0.03 *M* = 30 mM), a PS TON of 1998 suggests that one glycerol molecule was oxidized 6-7 times on
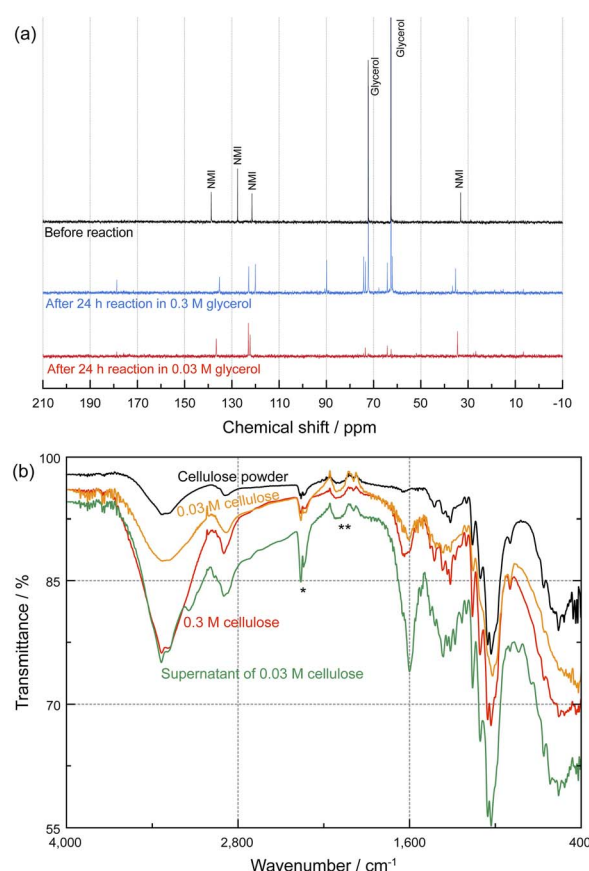

Fig. 6 (a) ^{13}C NMR spectra of reaction supernatants obtained by ultracentrifugation of the reaction mixtures containing **DDSP-4b**, 15 mM TEMPO, 50 mM NMI and 0.3 (blue) or 0.03 M (red) glycerol aqueous solution. The black line in panel (a) shows the spectrum of reaction solution before light irradiation. (b) IR spectra of the precipitates isolated by ultracentrifugation of the reaction mixtures containing **DDSP-4a**, 15 mM TEMPO, 50 mM NMI and 0.03 (orange) or 0.3 M (red) cellulose dispersion in comparison with the spectrum of cellulose powder (black). The green line shows the spectrum of the precipitate obtained by evaporation of the reaction supernatant containing 0.03 M cellulose. Vibrations of CO_2 in air and background noise derived from the diamond ATR prism are marked by asterisks.

average *via* the TEMPO mediator during 24 h of photocatalytic H_2 production using **DDSP-4b**. Similarly, the estimated PS TON value of ~3703 for the 0.3 M glycerol solution suggests that

glycerol underwent only 1.2 one-electron oxidation reactions per molecule, which is consistent with the persistence of glycerol peaks in the ^{13}C NMR spectra after 24 h of photocatalytic reaction (Fig. 6a). Notably, in addition to several new peaks near the original glycerol peaks, a singlet at 178 ppm was clearly observed, suggesting the formation of a carboxyl group *via* the TEMPO-mediated oxidation of glycerol. Furthermore, the two supernatant solutions with distinct glycerol concentrations exhibited markedly differing spectra, indicating that the degree of glycerol oxidation differed, as suggested by the dissimilar PS-TON values.

Oxidation of the cellulose dispersion was confirmed based on the IR spectra of the reaction powder isolated by ultracentrifugation (50 000 rpm for 15 min) of the reaction mixture (Fig. 6b). The spectra of the powders obtained from 0.03 and 0.3 M cellulose dispersions clearly exhibited a new peak at ~1600 cm^{-1} in comparison to that of cellulose powder. This new peak was assigned to the carboxylate group formed *via* TEMPO-catalysed oxidation, according to a previous report.[18] A similar spectral change was also found for the sample obtained from the reaction with wood pellets (Fig. S8). It should be noted that the supernatant obtained by ultracentrifugation of the reaction mixture exhibited strong Tyndall scattering (inset photo of Fig. 5b). Because such scattering was negligible in the supernatant isolated from the glycerol solution (inset photograph in Fig. 5a), the Tyndall scattering likely did not originate from **DDSP-4a** but from the oxidation product(s) generated *via* TEMPO-catalysed cellulose oxidation. Dynamic light scattering analysis revealed the size of oxidation products in the supernatant to be ~66.9 ± 27.7 nm, which is two orders of magnitude smaller than the particle size of the 0.03 M cellulose dispersion without a photocatalytic reaction (Fig. S9). The Brownian motion of oxidized cellulose aggregates several micrometres in size was clearly observed under a microscope (see Movie S1). Furthermore, the IR spectrum of the solid obtained by evaporation of the supernatant was comparable to that of the reaction powder, as well as a significantly stronger carboxylate peak at 1600 cm^{-1} (green line in Fig. 6b). Thus, we concluded that the cellulose powder was oxidized by TEMPO as an electron/proton source for photocatalytic H$_2$ production using **DDSP-4a** and gradually converted into cellulose nanofibers.

3.6 H$_2$ evolving photodissolution of cellulose paper

Because photocatalytic H$_2$ production from the cellulose dispersion was achieved using our **PRCC** system comprising **DDSP-n** and TEMPO, we further fabricated a **PRCC-n** paper by simply drop-casting the **DDSP-n** aqueous dispersion onto a cellulose filter paper (Fig. 7b, see the Experimental section in the SI for details). Fig. 7a shows the results of photocatalytic H$_2$ production using **PRCC-1a** or **-5b** papers in a 15 mM TEMPO and 50 mM NMI mixed aqueous solution. The estimated amounts of H$_2$ evolved, PS TON, PS TOF during 24 h of reaction, and *i*AQY are listed in Table 4. Both **PRCC-1a** and **-5b** papers successfully produced H$_2$ without the addition of any substrate under blue light irradiation, and H$_2$ bubbles that evolved from the surface of the **PRCC-1a** paper were also observed by the
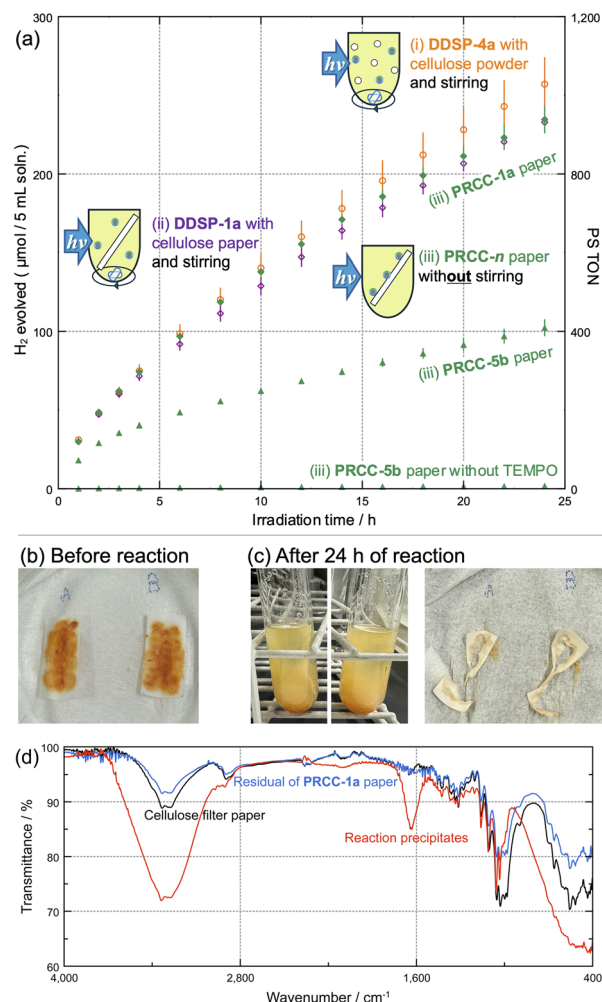

Fig. 7 (a) Photocatalytic H$_2$ production reactions of **PRCC-n** (*n* = **1a** and **5b**) papers in [TEMPO] = 15 mM and [NMI] = 50 mM mixed aqueous solution. Inset schematic images show three different reaction methods: (i) orange circles, (the same data are shown in Fig. 5b), **DDSP-4a** with 0.03 M cellulose powder, (ii) purple diamonds, **DDSP-1a** with 55 mg cellulose paper, and (iii) green symbols, **PRCC-n** (*n* = **1a**, **5b**) paper without stirring. The Ru(ɪɪ) dye concentration of all the reactions was adjusted to 100 μM (initial pH = 9) under blue-light irradiation (λ = 467 ± 30 nm; 550 mW). Panels (b) and (c) show photographs of two **PRCC-1a** papers before and after 24 h of reaction, respectively. (d) IR spectra of the reaction precipitates (red) and residue of **PRCC-1a** paper (blue) after 24 h of reaction. The black line shows the spectrum of cellulose filter paper used for **PRCC-1a** paper preparation.

naked eye (see Movie S2). In contrast, H$_2$ bubbles were hardly observed when the cellulose paper was replaced by a polytetrafluoroethylene polymer membrane, suggesting the important role of cellulose paper for photocatalytic H$_2$ production. The evolved amount of H$_2$ after 24 h was 2.3-fold larger for **PRCC-1a** than for **PRCC-5b** (Table 4, entries 3 and 4). This activity trend, **1a** > **5b**, qualitatively agreed with the results for the 0.1 M cellulose dispersion condition (Table 2, *n* = **1a**, **5b**), suggesting that the photocatalytic activity of **DDSP-n** is the dominant factor for the H$_2$ evolving **PRCC-n** paper system. Surprisingly, the estimated *i*AQY for **PRCC-1a** paper (0.77%) was

Table 4 Results of photocatalytic H$_2$ production using **PRCC-1a** and **-5b** papers in 15 mM TEMPO, 50 mM NMI aqueous solution[a]

Entry	Photocatalyst/substrate	Evolved H$_2$ [μmol]	PS TON	PS TOF	iAQY [%]
1[b]	**DDSP-4a**/24 mg cellulose powder	257.0 ± 16.8	1028	42.83	0.80
2	**DDSP-1a**/55 mg cellulose paper	232.9 ± 3.94	931	38.81	0.77
3	**PRCC-1a** paper	234.7 ± 8.50	939	39.12	0.77
4	**PRCC-5b** paper	102.3 ± 5.00	409	17.05	0.47
5	**PRCC-5b** paper without TEMPO	1.70 ± 0.11	6.82	0.28	<0.01

[a] Reaction conditions: [PS] = 100 μM in total, [TEMPO] = 15 mM, [NMI] = 50 mM aqueous solution (pH 9), λ_{ex} = 467 ± 30 nm (550 mW). The reaction solution was purged by bubbling Ar through it for 1 h prior to light irradiation. Numerical values represent the average of more than three experiments. Definitions: PS, photosensitizer; TON, turnover number over 24 h of reaction; TOF, turnover frequency over 24 h of reaction; iAQY, apparent quantum yield during the initial 1 h of reaction. [b] The same data are listed in Table 3, entry 6.

similar to that of the mixed dispersion of **DDSP-4a** and 0.03 M cellulose powder (0.80%) and to that of the **DDSP-1a** dispersion with the same-weight cellulose paper (0.77%, Table 4, entries 1–3), despite **DDSP-1a** nanoparticles being immobilized on the cellulose paper surface and the absence of magnetic stirring. These comparable activities suggest that the drop-casting of **DDSP-1a** onto cellulose paper minimizes the diffusion distance of the TEMPO mediator between the **DDSP-1a** photocatalyst and the cellulose substrate, thereby promoting TEMPO catalytic and electron-mediating cycles. In fact, the **PRCC-1a** paper dissolved in the area where the **DDSP-n** dispersion was drop-cast (Fig. 7b and c). This partial photodissolution of the cellulose paper indicated that the **DDSP-n**-drop-cast cellulose itself acted as a hydrogen source for H$_2$ production using **DDSP-n**. Although **DDSP-n** was directly adsorbed on the surface of the cellulose paper, the **PRCC-5b** paper produced negligible H$_2$ in the absence of TEMPO (Table 4, entry 5). Thus, TEMPO in solution acts as an electron mediator and molecular catalyst by permeating the **PRCC-n** paper. Although photocatalytic H$_2$ production was also observed when cotton sponge was used as the substrate instead of cellulose paper (Fig. S10), the amount of evolved H$_2$ after 24 h of reaction was approximately two-fold lower. Considering that the **PRCC-4a** sponge containing the generated H$_2$ bubbles was pushed above the aqueous surface after 24 h of reaction (inset of Fig. S10), the TEMPO catalytic cycle in the aqueous phase was plausibly suppressed by the gaseous H$_2$ bubbles. The residue of **PRCC-1a** paper and the reaction precipitates were analysed using IR spectroscopy (Fig. 7d). Based on the estimated PS TON for the **PRCC-1a** paper (939) and the molar ratio of the Ru(II) dye and the cellulose monomer unit in the **PRCC-1a** paper (1 : 678), the cellulose substrate was considered to undergo at least one one-electron oxidation reaction per monomer on average. However, the residue corresponding to the area minimally drop-cast with **DDSP-1a** exhibited an almost identical spectrum to that of the cellulose filter paper, suggesting that TEMPO-mediated oxidation occurred negligibly in the area without **DDSP-1a** loading. In contrast, a strong COO$^-$ vibration peak originating from the oxidized cellulose was observed at ~1600 cm^{-1} for the reaction precipitate. These two spectroscopic results further support that the **DDSP-1a**-loaded section of the **PRCC-1a** paper was preferentially oxidized over the unloaded section by TEMPO mediators that permeated the paper, resulting in its preferential dissolution.

4 Conclusions

In this study, 12 different dual-dye-sensitized photocatalysts (**DDSP-n**) comprising Pt-cocatalyst-loaded TiO$_2$ nanoparticles were synthesized by varying the Ru(II) dye immobilization order, Ru(II) dye (**RuP^6** and **RuCP^6**) concentrations, and Zr^{4+} and Hf^{4+} salt concentrations to identify the dominant structural features of the photoredox cascade catalyst (**PRCC**) for photocatalytic H$_2$ production coupled with TEMPO-catalysed biomass (glycerol and cellulose) reforming. The combination of systematic photocatalytic activity evaluation and machine learning analysis revealed that the most crucial factor for the photocatalytic activity of the **PRCC** system is the immobilization order of the two Ru(II) dyes to fabricate a suitable photoredox cascade structure for efficient charge separation, followed by the binding of Zr^{4+} cations, which is necessary for the stable formation of the **RuCP^6**-Zr^{4+}-**RuP^6** dual-dye layer on the Pt-TiO$_2$ nanoparticle surface. To achieve high photocatalytic activity, sufficient loading of the inner **RuP^6** dye (directly anchored on the TiO$_2$ nanoparticle surface) is essential to ensure full coverage of the TiO$_2$ nanoparticle surface, whereas increasing the loading of the outer **RuCP^6** dye would not necessarily improve activity. The optimization process led to improved performances, with **DDSP-1a** displaying a higher apparent quantum yield (iAQY = 2.59 and 1.47% at 467 nm excitation in a 0.1 M substrate, corresponding to 20 998 and 9577 μmol g^{-1}.h.) than a state-of-the-art photocatalyst for cellulose photoreforming in the presence of a strong base (Table S3), without the use of strong acids/bases. The TEMPO$^+$ cation, photocatalytically produced by the **DDSP-n** nanoparticles, successfully converted cellulose powder and paper into cellulose nanofibers as the oxidation product. This finding offers significant economic benefits in terms of practical cellulose photoreforming, as it enables the simultaneous production of hydrogen and high-value-added oxidation products such as cellulose nanofibers. Furthermore, a H$_2$-evolving **PRCC-n** paper was fabricated by drop-casting a **DDSP-n** aqueous dispersion onto a cellulose filter paper surface. Surprisingly, the photocatalytic H$_2$ evolution activity of the **PRCC-n** paper (iAQY = 0.77% for **PRCC-1a**) without magnetic stirring was almost comparable to that of **DDSP-n** in a 30 mM cellulose aqueous dispersion with magnetic stirring, suggesting the positive effect of loading **DDSP-n** nanoparticles directly onto the surface of cellulose paper on the photo-induced charge separation with

a TEMPO mediator/catalyst. Because photocatalytic H_2 production was achieved using cellulose in various states (fine powder, paper, sponge, and wood pellets), we believe that the findings of this study will open a new avenue not only for green H_2 production from sustainably available cellulosic resources but also for cost-effective cellulose nanofiber production.

Author contributions

A. K. conceived the idea and carried out all the synthesis and evaluation of photocatalytic activity. A. M. visualized the Brownian motion of oxidized cellulose. K. T. performed the machine-learning analysis. A. K. prepared the manuscript and A. M. and K. T. helped in the revision of the manuscript. The manuscript was written through contributions of all authors. All authors have given approval to the final version of the manuscript.

Conflicts of interest

There are no conflicts to declare.

Data availability

The data supporting this article have been included as part of the SI.

SI available: Details of experiments and machine-learning analysis; UV-vis absorption spectra of all supernatant solutions obtained in the syntheses of **DDSP-*n***; particle diameter distributions estimated by dynamic light scattering for the supernatant of the reaction mixture **DDSP-4a** with 0.3 M cellulose; photocatalytic H_2 production using **PRCC-4a** sponge. Movies of microscopic observation of the Brownian motion of oxidized cellulose produced by the photocatalytic reaction using **DDSP-4a** and photocatalytic H_2 production using **PRCC-1a** paper. See DOI: **https://doi.org/10.1039/d5su00054h**.

Acknowledgements

Notes and references

1 S. N. Naik, V. V. Goud, P. K. Rout and A. K. Dalai, *Renewable Sustainable Energy Rev.*, 2010, **14**, 578–597.

2 D. Klemm, B. Heublein, H.-P. Fink and A. Bohn, *Angew. Chem., Int. Ed.*, 2005, **44**, 3358–3393.

3 F. H. Isikgora and C. R. Becer, *Polym. Chem.*, 2015, **6**, 4497–4559.

4 H. Zhu, W. Luo, P. N. Ciesielski, Z. Fang, J. Y. Zhu, G. Henriksson, M. E. Himmel and L. Hu, *Chem. Rev.*, 2016, **116**, 9305–9374.

5 L. T. Mika, E. Cséfalvay and Á. Németh, *Chem. Rev.*, 2018, **118**, 505–613.

6 F. Wang, D. Ouyang, Z. Zhou, S. J. Page, D. Liu and X. Zhao, *J. Energy Chem.*, 2021, **57**, 247–280.

7 W. Deng, Y. Feng, J. Fu, H. Guo, Y. Guo, B. Han, Z. Jiang, L. Kong, C. Li, H. Liu, P. T. T. Nguyen, P. Ren, F. Wang, S. Wang, Y. Wang, Y. Wang, S. S. Wong, K. Yan, N. Yan, X. Yang, Y. Zhang, Z. Zhang, X. Zeng and H. Zhou, *Green Energy Environ.*, 2023, **8**, 10–114.

8 T. Shen and S. Gnanakaran, *Biophys. J.*, 2009, **96**, 3032–3040.

9 A. S. Gross and J.-W. Chu, *J. Phys. Chem. B*, 2010, **114**, 13333–13341.

10 T. Minowa, F. Zhen and T. Ogi, *J. Supercritical Fluids*, 1998, **13**, 253–259.

11 J. Cai and L. Zhang, *Macromol. Biosci.*, 2005, **5**, 539–548.

12 T. Budtova and P. Navard, *Cellulose*, 2016, **23**, 5–55.

13 N. R. Quiroz, A. M. D. Padmanathan, S. H. Mushrif and D. G. Vlachos, *ACS Catal.*, 2019, **9**, 10551–10561.

14 P. Hu, H. Li, Z. Xue, D. Wu, Y. Hu, L. Li, C. Hu and L. Zhu, *ACS Sustainable Chem. Eng.*, 2024, **12**, 393–404.

15 S. Van de Vyver, J. Geboers, P. A. Jacobs and B. F. Sels, *ChemCatChem*, 2011, **3**, 82–94.

16 H. Kobayashi, T. Komanoya, S. K. Guhaa, K. Hara and A. Fukuoka, *Appl. Catal., A*, 2011, **409–410**, 13–20.

17 A. Isogai and Y. Kato, *Cellulose*, 1998, **5**, 153–164.

18 D. S. Perez, S. Montanari and M. R. Vignon, *Biomacromolecules*, 2003, **4**, 1417–1425.

19 A. Isogai, T. Saito and H. Fukuzumi, *Nanoscale*, 2011, **3**, 71–85.

20 S. J. Eichhorn, A. Dufresne, M. Aranguren, N. E. Marcovich, J. R. Capadona, S. J. Rowan, C. Weder, W. Thielemans, M. Roman, S. Renneckar, W. Gindl, S. Veigel, J. Keckes, H. Yano, K. Abe, M. Nogi, A. N. Nakagaito, A. Mangalam, J. Simonsen, A. S. Benight, A. Bismarck, L. A. Berglund and T. Peijs, *J. Mater. Sci.*, 2010, **45**, 1–33.

21 K. J. Nagarajan, N. R. Ramanujam, M. R. Sanjay, S. Siengchin, B. Surya Rajan, K. Sathick Basha, P. Madhu and G. R. Raghav, *Polym. Compos.*, 2021, **42**, 1588–1630.

22 M. F. Kuehnel and E. Reisner, *Angew. Chem., Int. Ed.*, 2018, **57**, 3290–3296.

23 X. Liu, X. Duan, W. Wei, S. Wang and B.-J. Ni, *Green Chem.*, 2019, **21**, 4266–4289.

24 J. Wang, P. Kumar, H. Zhao, M. G. Kibria and J. Hu, *J. Green Chem.*, 2021, **23**, 7435–7457.

25 X. Xu, L. Shi, S. Zhang, Z. Ao, J. Zhang, S. Wang and H. Sun, *Chem. Eng. J.*, 2023, **469**, 143972.

26 M. Ashraf, N. Ullah, I. Khan, W. Tremel, S. Ahmad and M. N. Tahir, *Chem. Rev.*, 2023, **123**, 4443–4509.

27 Y. Wu, T. Sakurai, T. Adachi and W. Wang, *Nanoscale*, 2023, **15**, 6521–6535.

28 A. Negi and K. K. Kesari, *Polymers*, 2023, **15**, 3671.

29 S. Feng, P. T. T. Nguyen, X. Ma and N. Yan, *Angew. Chem., Int. Ed.*, 2024, **63**, e202408504.

30 T. Kawai and T. Sakata, *Nature*, 1980, **286**, 474–476.

31 A. Speltini, M. Sturini, D. Dondi, E. Annovazzi, F. Maraschi, V. Caratto, A. Profumo and A. Buttafava, *Photochem. Photobiol. Sci.*, 2014, **13**, 1410–1419.

32 G. Zhang, C. Ni, X. Huang, A. Welgamage, L. A. Lawton, P. K. J. Robertson and J. T. Irvine, *Chem. Commun.*, 2016, **52**, 1673–1676.

33 L. Zhang, W. Wang, S. Zeng, Y. Su and H. Hao, *Green Chem.*, 2018, **20**, 3008–3013.

34 J. Zou, G. Zhang and X. Xu, *Appl. Catal., A*, 2018, **563**, 73–79.

35 L. Lan, H. Daly, Y. Jiao, Y. Yan, C. Hardacre and X. Fan, *Int. J. Hydrogen Energy*, 2021, **46**, 31054–31066.

36 D. W. Wakerley, M. F. Kuehnel, K. L. Orchard, K. H. Ly, T. E. Rosser and E. Reisner, *Nat. Energy*, 2017, **2**, 17021.

37 D. S. Achilleos, W. Yang, H. Kasap, A. Savateev, Y. Markushyna, J. R. Durrant and E. Reisner, *Angew. Chem., Int. Ed.*, 2020, **59**, 18184–18188.

38 H. Nagakawa and M. Nagata, *ACS Appl. Energy Mater.*, 2021, **4**, 1059–1062.

39 H. Kasap, D. S. Achilleos, A. Huang and E. Reisner, *J. Am. Chem. Soc.*, 2018, **140**, 11604–11607.

40 X. Wu, H. Zhao, M. A. Khan, P. Maity, T. Al-Attas, S. Larter, Q. Yong, O. F. Mohammed, M. G. Kibria and J. Hu, *ACS Sustainable Chem. Eng.*, 2020, **8**, 15772–15781.

41 C. Rao, M. Xie, S. Liu, R. Chen, H. Su, L. Zhou, Y. Pang, H. Lou and X. Qiu, *ACS Appl. Mater. Interfaces*, 2021, **13**, 44243–44253.

42 E. Wang, A. Mahmood, S.-G. Chen, W. Sun, T. Muhmood, X. Yang and Z. Chen, *ACS Catal.*, 2022, **12**, 11206–11215.

43 B. O'Regan and M. Grätzel, *Nature*, 1991, **353**, 737–740.

44 A. Hagfeldt, G. Boschloo, L. Sun, L. Kloo and H. Pettersson, *Chem. Rev.*, 2010, **110**, 6595–6663.

45 F. Bella, C. Gerbaldi, C. Barolo and M. Grätzel, *Chem. Soc. Rev.*, 2015, **44**, 3431–3473.

46 T. J. Meyer, M. V. Sheridan and B. D. Sherman, *Chem. Soc. Rev.*, 2017, **46**, 6148–6169.

47 J. C. Wang, S. P. Hill, T. Dilbeck, O. O. Ogunsolu, T. Banerjee and K. Hanson, *Chem. Soc. Rev.*, 2018, **47**, 104–148.

48 A. Kobayashi, S. Takizawa and M. Hirahara, *Coord. Chem. Rev.*, 2022, **467**, 214624.

49 A. Kobayashi, *ChemSusChem*, 2025, **18**, e202400688.

50 K. Hanson, D. A. Torelli, A. K. Vannucci, M. K. Brennaman, H. Luo, L. Alibabaei, W. Song, D. L. Ashford, M. R. Norris, C. R. K. Glasson, J. J. Concepcion and T. J. Meyer, *Angew. Chem., Int. Ed.*, 2012, **51**, 12782–12785.

51 B. H. Farnum, K.-R. Wee and T. J. Meyer, *Nat. Chem.*, 2016, **8**, 845–852.

52 R. N. Sampaio, L. Troian-Gautier and G. J. Meyer, *Angew. Chem., Int. Ed.*, 2018, **57**, 15390–15394.

53 A. Kobayashi, *Angew. Chem., Int. Ed.*, 2023, **62**, e202313014.

54 S. Gonuguntla, R. Kamesh, U. Pal and D. Chatterjee, *J. Photochem. Photobiol., C*, 2023, **57**, 100621.

55 Y.-S. Lai and Y.-H. Su, *ACS Agric. Sci. Technol.*, 2022, **2**, 615–624.

56 H. Park, W. Choi and M. R. Hoffmann, *J. Mater. Chem.*, 2008, **18**, 2379–2385.

57 M. R. Norris, J. J. Concepcion, C. R. K. Glasson, Z. Fang, A. M. Lapides, D. L. Ashford, J. L. Templeton and T. J. Meyer, *Inorg. Chem.*, 2013, **52**, 12492–12501.

58 N. Yoshimura, A. Kobayashi, M. Yoshida and M. Kato, *Chem. Eur. J.*, 2020, **26**, 16939–16946.

59 G. Varoquaux, L. Buitinck, G. Louppe, O. Grisel, F. Pedregosa, A. Mueller, *GetMobile: Mobile Computing and Communications*, 2015, **19**, 29–33.

60 S. A. Trammell, J. A. Moss, J. C. Yang, B. M. Nakhle, C. A. Slate, F. Odobel, M. Sykora, B. W. Erickson and T. J. Meyer, *Inorg. Chem.*, 1999, **38**, 3665–3669.

61 M. D. Brady, L. Troian-Gautier, T. C. Motley, M. D. Turlington and G. J. Meyer, *ACS Appl. Mater. Interfaces*, 2019, **11**, 27453–27463.

© 2025 The Author(s). Published by the Royal Society of Chemistry